Constraining Crustal Properties with Bayesian Joint Inversion of Vertical and Radial Teleseismic P-wave Coda Autocorrelations

Mehdi Tork Qashqai[1,1,1,1] and Erdinc Saygin[2,2,2,2]

[1]Deep Earth Imaging, Future Science Platform, The Commonwealth Scientific and Industrial Research Organization (CSIRO)
[2]CSIRO

November 30, 2022

Abstract

The sensitivity of seismic compressional and shear waves and their velocity ratios to rock lithology, pore fluids, and high-temperature materials makes these parameters very useful for constraining the physical state of the crust. In this study, we develop a joint inversion approach utilizing both radial and vertical components' autocorrelations of teleseismic P-wave coda for imaging the crust by simultaneously characterizing the crustal Vp, Vs and Vp/Vs ratio. Autocorrelations of the radial and vertical components contain P and S waves that are reflected back from the subsurface. Therefore, joint inversion of them can account for the variations of both Vp and Vs, and consequently, the Vp/Vs ratio. Synthetic inversions show significant improvement in the estimation of these parameters compared to those from the inversion of either, receiver functions or the autocorrelation of the vertical component. The velocity models inferred from the application of the approach on teleseismic data recorded along a north-south passive seismic profile (BILBY experiment) in central Australia reveal crustal-scale structures that clearly separate crustal domains. We found a thick crust (between 43 km and 57 km) along the BILBY profile. The general trend of the Moho structure imaged from the joint inversion corresponds well with the change of the reflectivity that is normally seen at the base of the crust and also with the Moho as interpreted using the deep seismic reflection profiling method.

Constraining Crustal Properties with Bayesian Joint Inversion of Vertical and Radial Teleseismic P-wave Coda Autocorrelations

Mehdi Tork Qashqai[1] **and Erdinc Saygin**[1,2]

[1]Deep Earth Imaging, Future Science Platform, CSIRO, Kensington, WA, Australia
[2]Department of Physics, School of Physics, Mathematics & Computing, Faculty of Engineering and Mathematical Sciences, University of Western Australia, Perth, WA, Australia

Key Points:

- We introduce a new joint inversion approach to estimate V_p, V_s simultaneously, and V_p/V_s ratio structures below a seismic station
- We jointly invert both the vertical and radial component autocorrelations of the teleseismic P-wave coda to image and characterize the crust
- The joint inversion provides better constraints than the inversion of either P receiver functions or the vertical component autocorrelation

Corresponding author: Mehdi Tork Qashqai, `mehdi.torkqashqai@csiro.au`

Abstract

The sensitivity of seismic compressional and shear waves and their velocity ratios to rock lithology, pore fluids, and high-temperature materials makes these parameters very useful for constraining the physical state of the crust. In this study, we develop a joint inversion approach utilizing both radial and vertical components' autocorrelations of teleseismic P-wave coda for imaging the crust by simultaneously characterizing the crustal V_p, V_s and V_p/V_s ratio. Autocorrelations of the radial and vertical components contain P and S waves that are reflected from the subsurface. Therefore, joint inversion of them can account for the variations of both V_p and V_s, and consequently, the V_p/V_s ratio. Synthetic inversions show significant improvement in the estimation of these parameters compared to those from the inversion of either, receiver functions or the autocorrelation of the vertical component. The velocity models inferred from the application of the approach to teleseismic data recorded along a north-south passive seismic profile (BILBY experiment) in central Australia reveal a distinct pattern of the Moho and the V_p/V_s variations across the crustal blocks/domain. The general trend of the Moho structure corresponds well with the change of the reflectivity that can normally be seen at the base of the crust and also with the Moho estimated from the previous studies including the deep seismic reflection profiling method. The V_p/V_s structure at depths greater than 10 km shows dominant high values beneath locations where the crustal domains interact (e.g., at transition from one domain to another).

Plain Language Summary

Understanding variations of the crustal P and S waves (V_p and V_s) can indicate rock lithology. Here, we introduce a new approach to estimate these wavespeeds simultaneously using vibrations from earthquakes recorded at seismic stations. Autocorrelations of the distant P-wave coda recorded on the vertical and radial components of a seismogram contain P- and S-wave reflections. Thus, they are sensitive to both the crustal wavespeeds and the crustal discontinuities. We test the feasibility of the new method with synthetic data, which reveals a substantial improvement in recovering the input V_p/V_s models. We then apply the approach to teleseismic waveforms recorded along a passive seismic experiment in central Australia to infer the crustal structure. The results reveal a distinct variation of the thickness of the crust and the V_p/V_s across geological units along the passive seismic line. The overall pattern of the crustal thickness variations also matches the change of reflectivity at the base of the crust. The inferred V_p/V_s model exhibits high V_p/V_s values at depths greater than 10 km beneath locations where the crustal domains interact.

1 Introduction

P-wave energy from a direct teleseismic source converts to S_v energy and vice versa across a sharp seismic boundary beneath a seismic station. This incoming energy contains multiple reflections from the underlying structure as well as peg-leg multiples and scattered and mode converted waves (coda). Teleseismic waves recorded on the vertical and radial components of a seismogram have been widely used to retrieve the impulse-response of the receiver-side structure by deconvolving the vertical component (P) from the horizontal or radial component (S_v). The resulting waveform is primarily sensitive to sharp V_s changes with depth and is commonly referred to as the "P receiver function" (hereafter RF), which represents the converted P- to S-wave energy directly beneath a seismic station (Ammon, 1991; Langston, 1979; Vinnik, 1977).

In addition to the RFs, single station autocorrelation and cross-correlation of teleseismic and ambient noise records can provide complementary constraints on the crustal properties beneath a seismic station, and have been successfully applied to teleseismic and ambient noise data for imaging crustal and lithospheric discontinuities (Ruigrok &

Wapenaar, 2012; Tibuleac & von Seggern, 2012; Gorbatov et al., 2013; Kennett., 2015; Kennett et al., 2015; Nishitsuji et al., 2016; Taylor et al., 2016; Sun & Kennett, 2016; Saygin et al., 2017; Oren & Nowack, 2017; Kim et al., 2017; Sun et al., 2018; Heath et al., 2018; Romero & Schimmel, 2018; Phạm & Tkalčić, 2018; Becker & Knapmeyer-Endrun, 2018, 2019; Tork Qashqai et al., 2019; Kim et al., 2019; Wang et al., 2020; Andrés et al., 2020; Casas et al., 2020). Claerbout (1968) showed that, by autocorrelating the records from a surface seismic station, the transmission response can be converted to a reflection response. Vinnik (1977) introduced a correlation-based approach to detect P-to-S converted waves (RFs) in the long period P-wave coda. Galetti and Curtis (2012) and Sun and Kennett (2016) showed that the cross-correlation of the vertical and radial components of a single-station could be considered an alternative implementation of the classical RFs (non-classical RFs).

Compared to the RFs, the autocorrelations of teleseismic P-wave coda recorded on the radial and vertical components of a seismogram contain additional information. The autocorrelations include both P- and P-to-S converted phases, whereas the RFs contains P-to-S phases primarily because the P-waves are canceled by the deconvolution operation in the RFs (Figure 1). Thus, both V_p and V_s can simultaneously be estimated by jointly inverting the radial and vertical components' autocorrelations. Recently, the autocorrelation of teleseismic P-wave coda recorded on the vertical component has been used within a Bayesian inversion framework to image the crust beneath Australia (Tork Qashqai et al., 2019). They confirmed the utility of this approach for estimating large-scale crustal properties such as V_p and Moho depths. However, to the best of our knowledge, the joint inversion of both radial and vertical components' autocorrelations has not yet been demonstrated. Such a joint inversion approach offers a framework to further reduce the uncertainties associated with the crustal seismic properties (V_p, V_S and V_p/V_s), and thus can provide an improved estimate of both V_p and V_s, and consequently the V_p/V_s ratio which provides an indication of the rock lithology beneath a seismic station.

In this study, we demonstrate the feasibility of the probabilistic joint inversion of radial and vertical components' autocorrelations for recovering the true 1-D structure (V_p, V_s and V_p/V_s) beneath a seismic station. We compare the results of the joint inversion with the single inversions of RFs and autocorrelation of the vertical component through a series of synthetic inversion tests. We then use this approach to image the crust beneath central Australia along a north-south seismic profile (BILBY seismic array) and compare our results with the results obtained from RF analysis (Sippl, 2016), Australian Moho Model-AusMoho (Kennett. et al., 2011), the deep seismic reflection profiling (Korsch & Doublier, 2016) and inversion of the vertical component autocorrelation (Tork Qashqai et al., 2019).

In the following sections, we briefly describe the autocorrelation and the RFs methods, each exploiting the arrival time delays of different phases.

2 Method

2.1 Autocorrelation of teleseismic P-wave coda

In this section we briefly describe the concept of autocorrelations of the vertical and radial components and the reader is referred to Frasier (1970), Langston (1979), Ammon (1991), Galetti and Curtis (2012), Sun and Kennett (2016), and Tauzin et al. (2019) for further details about the RF, cross-correlation and autocorrelation of components and their relationships.

In a plane-layered medium, when a steep incident plane P-wave from a distant earthquake (epicentral distances $\sim 30°$ - $90°$) impinges on an interface in the subsurface (e.g., Moho), the seismogram on the surface records direct P-wave energy, its direct P-to-S conversion phase, its peg-leg multiples and scattered waves including free-surface related multiples (Figure 1). The recorded teleseismic waveforms on the horizontal and vertical components of a seismogram can be processed to obtain the impulse-response of the subsurface structure in the forms of RFs and autocorrelations.

Claerbout (1968) showed that for plane waves impinging at normal incidence to a horizontally stratified acoustic medium with a free surface, the positive or negative part of the autocorrelation of the acoustic transmission response corresponds to the reflection response of the Earth beneath that station. We further illustrate this in Figure 1, where for simplicity, we consider a simple synthetic 1-D Earth model including one crustal layer over a half-space. The autocorrelations of the vertical or radial components of a seismometer contain seismic waves reflected back from the free-surface, such as $Pppmp$ and $Ppsms$ (Figure 1). These reflections have the same delay times as PmP and SmS that are reflected back from the bottom of the model (e.g., the Moho) and can be thought of as the Earth's response to a virtual source co-located with the receiver (zero-offset) at the surface of the Earth (Figure 1). RFs are generated through the deconvolution of the vertical component from the radial component, thus only includes P-to-S phases, and the PmP phase has been removed by deconvolution (Figure 1). As seen from Figure 1, the autocorrelations of both the radial and vertical components not only have the P-to-S phases that exist in the RF but also contain the PmP phase, and are able to carry additional information from the subsurface. Therefore, the inverse modeling of autocorrelation waveforms provides a means of subsurface characterization.

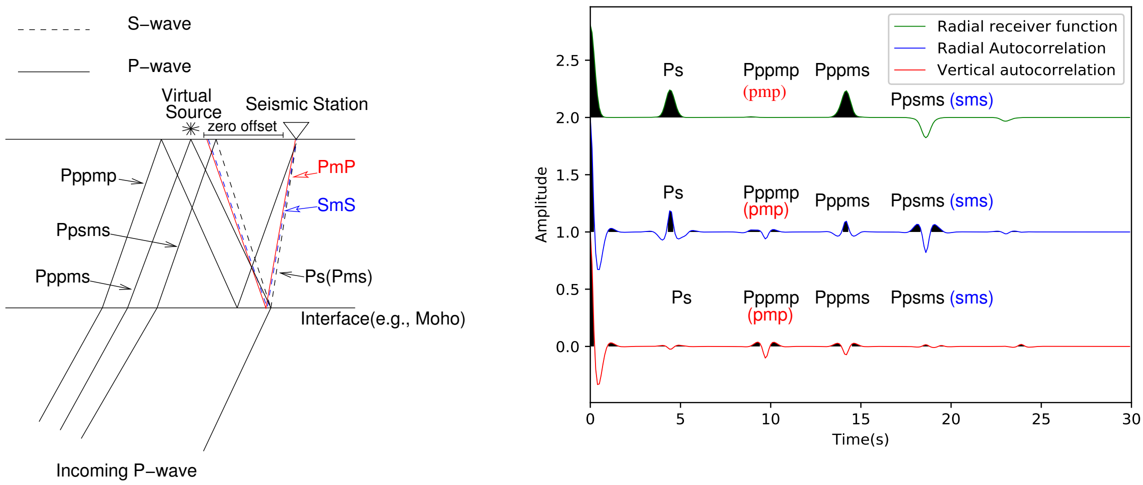

Figure 1. Left: schematic representation of a teleseismic plane wave impinging on a layer. Thickness, V_p, V_s, V_p/V_s of the layer are 35 km, 6.65 km/s, 3.69 km/s and 1.8, respectively. Note that the diagram is horizontally exaggerated to highlight the seismic phases. Right: shows the delay times of the main phases and the free-surface related multiples associated with the receiver function (top), the autocorrelation of the radial (middle) and vertical (bottom) components which were obtained using the model shown on the left. Capital P denotes upcoming P-wave in the half-space/mantle. All the lower case letters denote p or s waves in the crust (upgoing and downgoing waves).

2.2 Bayesian Inversion Framework

In the Bayesian inverse problem the general solution in the model space $\mathbf{m}$ is a task of combining pieces of information (expressed in the forms of probability density functions-PDF) provided by i) some measurements (observations/data space $\mathbf{d}$), ii) a model or theory that can predict observations [forward problem $g(\mathbf{m})$], and iii) some *a priori* knowledge about the model $\rho(\mathbf{m})$ into the *a posteriori* knowledge, the posterior PDF $\sigma_M(\mathbf{m})$(Tarantola, 2005; Debski, 2010). The data space is described as the space of all conceivable observations (e.g., instrumental responses) and is given by a probability density function (PDF) with the mean value at the center of this distribution and a width (dispersion, standard deviation) that quantifies the uncertainty of the observed data and their correlations (Tarantola, 2005; Mosegaard & Hansen, 2016). It has been shown that this posterior PDF under assumption that the data space is a linear space can be proportional to (Tarantola, 2005)):

$$\sigma_M(\mathbf{m}) \propto \rho(\mathbf{m})L(\mathbf{m}), \tag{1}$$

where $L(\mathbf{m})$ represents the likelihood function and gives a measure of how well a model $\mathbf{m}$ explains or fits the data ($\mathbf{d}$). If all uncertainties of the problem are approximated by the Gaussian model, $\sigma(\mathbf{m})$ can be given by (Tarantola, 2005; Gouveia & Scales, 1998):

$$\sigma_M(\mathbf{m}) \propto \exp(-S(\mathbf{m})), \tag{2}$$

where $S(\mathbf{m})$ is sum of squares:

$$S(\mathbf{m}) = \frac{1}{2}\left[\left(g(\mathbf{m}) - d_{obs}\right)^t C_D^{-1}\left(g(\mathbf{m}) - d_{obs}\right)\right] \tag{3}$$

C_D in equation (3) represents covariance matrix which is sum of the modelization and observational uncertainties (Gouveia & Scales, 1998; Tarantola, 2005). The modelization uncertainties are often neglected because they are difficult to quantify. In the case of independent uncertainties (the data covariance matrix is diagonal), equation (3) can be generalized to the following form (Tarantola, 2005) for joint inversion of autocorrelations of the vertical and radial components:

$$\sigma_M(\mathbf{m}) \propto \exp\left(-\frac{1}{2}\left[w_z\sum_{i=1}^{N}\left(\frac{d_i - g_i(\mathbf{m})}{\sigma_d^i}\right)^2 + w_r\sum_{j=1}^{N}\left(\frac{d_j - g_j(\mathbf{m})}{\sigma_d^j}\right)^2\right]\right) \tag{4}$$

The term inside the exponential is the misfit function, the total number of data points is N, i and j refer to data points in the autocorrelations of the vertical and radial components, respectively, $g(m)$ denotes calculated or predicted data at each point i and j (forward problem) and σ_d^i and σ_d^j are 1σ uncertainties for each data point of the autocorrelation waveforms along the time axis, w_z and w_r are weighting values that can be used for the optimization of the inversion. In this study, w_z and w_r are set to one.

In practice, the Markov Chain Monte Carlo (MCMC) techniques are usually employed to estimate the general solution of the inversion. MCMC methods are a class of techniques used to sample a model space and can estimate a range of models that fit the data well in the form of the posterior distribution. We adopted the Delayed Rejection Adaptive Metropolis algorithm (DRAM) (Haario et al., 2006). DRAM is a Markov Chain Monte Carlo (MCMC) approach and has been widely used in many hydrological and geophysical model parameter estimation problems (Smith & Marshall, 2008; Ball et al., 2014; Afonso et al., 2016; Tork Qashqai et al., 2018). It combines the Adaptive Metropolis (AM) (Haario et al., 2001) with Delayed Rejection (DR) (Mira, 2001) algorithms. DR provides a mechanism for drawing alternative samples when the current sample is rejected in the standard Metropolis-Hastings algorithm (Tierney, 1994), thus improving the efficiency of the sampling by reducing the number of rejections. In the AM, to reduce the sampling of low probability areas in the model space, the algorithm updates the covariance matrix of the chain (after a non-adaption period) using all the previously accepted samples. This process can be iterated at regular intervals.

In this study, the total number of simulations per station is 400,000. The non-adaptation time includes 150,000 iterations (or samples), and the proposal distribution of the model is updated after the non-adaptation time every 3,000 samples.

2.3 Parameterization and Forward Problem

The 1-D crust below each seismic station is parameterized with a stack of ten plane-parallel homogeneous crustal layers bounded at the base of the crust by a homogeneous upper mantle as a half-space. We use a step function parameterization, including ten crustal layers for joint inversion of the field data. This allows the inversion to capture the potential gradational transition across crustal discontinuities, including the crust-mantle boundary (Moho) that exist in central Australia (Kennett. et al., 2011). Each crustal layer is described by three parameters: density (ρ), thickness variation (ΔH) and V_p/V_s. Upper mantle parameters (V_p/V_s and density). As we applied a move out correction to the observed autocorrelations assuming a reference slowness of 0.065 s/km (see section 4.2), the slowness parameter is allowed to vary only between 0.064 and 0.066 km/s (fixed around the reference slowness).

The first step in the MCMC inversion is to randomly draw values for the main unknown parameters from their prior distributions (Table 1). Note that for the perturbation of crustal thicknesses in our inversion framework, the MCMC algorithm needs an initial crustal thickness model to perturb. Here, we assume that the initial crustal thickness below each seismic station is 40 km and includes ten layers, each with an equal thickness of 4 km. To perturb the initial crustal thickness model, the initial thickness of each layer is randomly perturbed (by the MCMC algorithm) using the random value drawn in the earlier step from the range of ΔH given in Table 1. In the next step, P-wave velocities for each layer (including the half-space) are estimated from the sampled random density values using the empirical Nafe-Drake curve (Ludwig et al., 1970; Brocher, 2005). The V_s value for each layer is then calculated from the computed V_p and the V_p/V_s values drawn by the MCMC algorithm.

The synthetic seismograms are computed using the reflectivity method of Kennett (1983) as implemented by Randall (1989). Autocorrelations of the vertical and radial components are calculated to estimate the synthetic reflection responses of the 1-D Earth beneath each station. A first-order Butterworth band-pass filter in the frequency range of 1 and 2 Hz is applied before and after the autocorrelation and amplitudes are normalized to unity.

Table 1. The list of all unknown parameters and priors.

Main parameters	Minimum	Maximum
Density in layer one (g/cm^3)	2.4	2.7
Density in layer two to layer five (g/cm^3)	2.65	2.85
Density in layer six to layer ten (g/cm^3)	2.7	3.0
V_p/V_s (in all crustal layers)	1.65	1.95
Δh in layer one to layer nine (km)	-4.0	4.0
Δh in layer ten (km)	-5.0	15.0
Density in the upper mantle/half-space (g/cm^3)	3.25	3.5
Slowness (s/km)	0.064	0.066

3 Synthetic Inversion Tests

To demonstrate the feasibility of the joint inversion framework, we run a series of inversion tests on synthetic autocorrelations and RFs generated using a synthetic 1-D Earth model consists of four crustal layers and a half-space. The aim is to invert these data using a ten-layer crust to recover the synthetic model (Figure 2 and Figure 3). We generate synthetic seismograms using the model and fifty random events with horizontal slowness values varying between 0.04 and 0.08 s/km. A small amount of Gaussian noise is added (with mean zero and standard deviation of 0.01) to the synthetic seismograms. Then, RFs, radial and vertical autocorrelations are generated from synthetic seismogram, the move-out correction is applied and all waveforms (for each data type) are stacked to obtain the stack of the data and their uncertainties. We performed the following three different inversion tests: 1) inversion of only RF, 2) inversion of only autocorrelation of the vertical component, and 3) the joint inversion of the vertical and radial component autocorrelations. Results are displayed in Figure 2 and Figure 3.

A ten-layered parameterization is chosen because we invert the field data using a ten-layered crust (next section), which improves data fitting. The mean values of the posterior distributions of V_p, V_s and V_p/V_s, as well as the true models, are given in Figure 2. Fits to the data are displayed in Figure 3, where the fit to synthetic data is reasonably well. Results suggest that the inversions of RFs or autocorrelation of the vertical component alone can provide reasonable estimates of the true V_s or V_p structures in a probabilistic sense, but they cannot fully recover the true V_p/V_s ratio. This to a large extent is because they are not sufficiently sensitive to either V_p or V_s and consequently a small deviation from the true values can lead to significant changes in the V_p/V_s ratio. The joint inversion of the radial and vertical components' autocorrelations, on the other hand, resolve a much better estimate of crustal properties, especially the V_p/V_s ratio, and reduces the non-uniqueness of the inversion solution. This is an important aspect of this joint inversion approach that we would like to emphasize here.

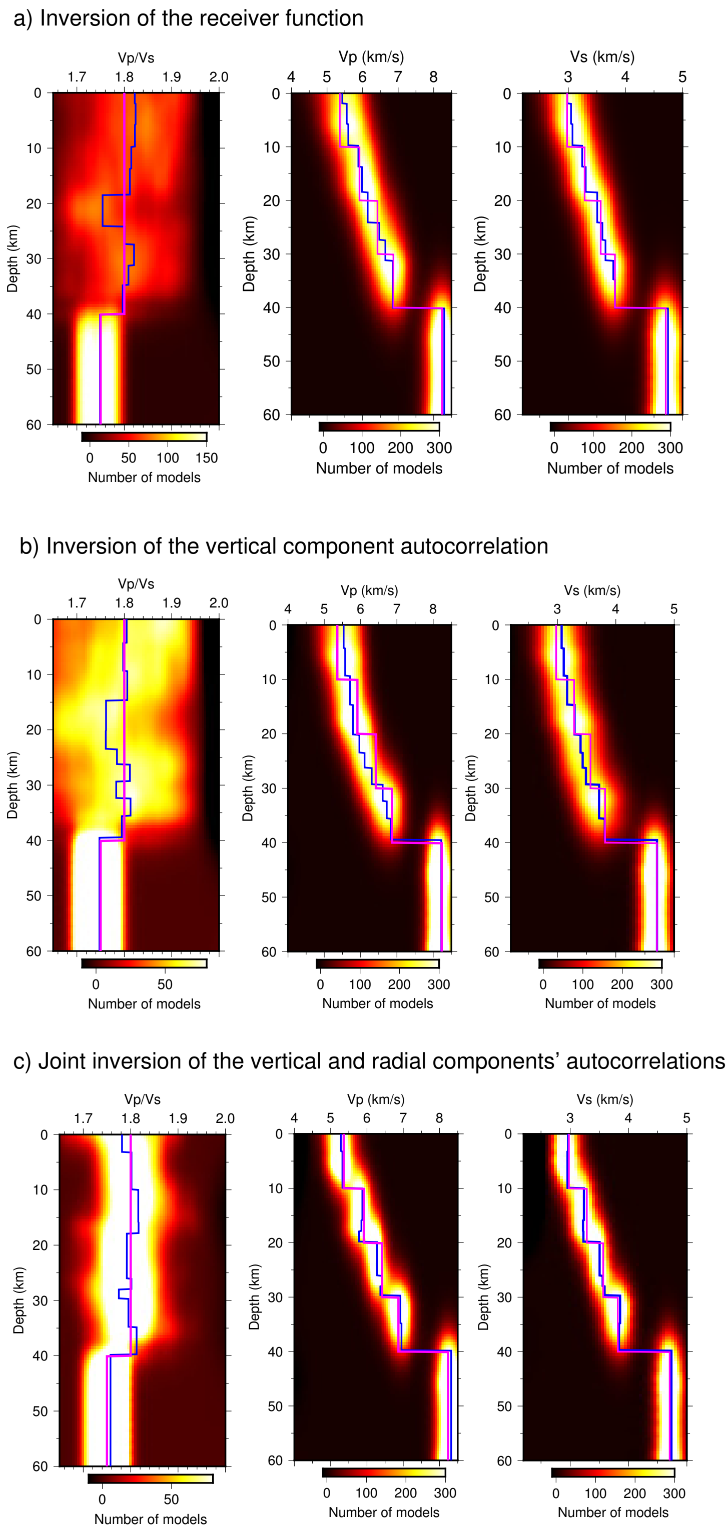

Figure 2. Synthetic inversions of a four-layered model with a ten-layered parameterization. Density plots of the posterior distribution of the V_p/V_s, V_p and V_s structures for a) inversion of the RF, b) inversion of the autocorrelation of the teleseismic P-wave coda recorded on the vertical component, c) joint inversion of autocorrelations of the teleseismic P-wave coda recorded on the vertical and radial components. High probability areas are shown with hot colors. Magenta profiles are true (synthetic) velocity, and V_p/V_s structures and the dark blue profiles indicate the mean of the posterior distribution.

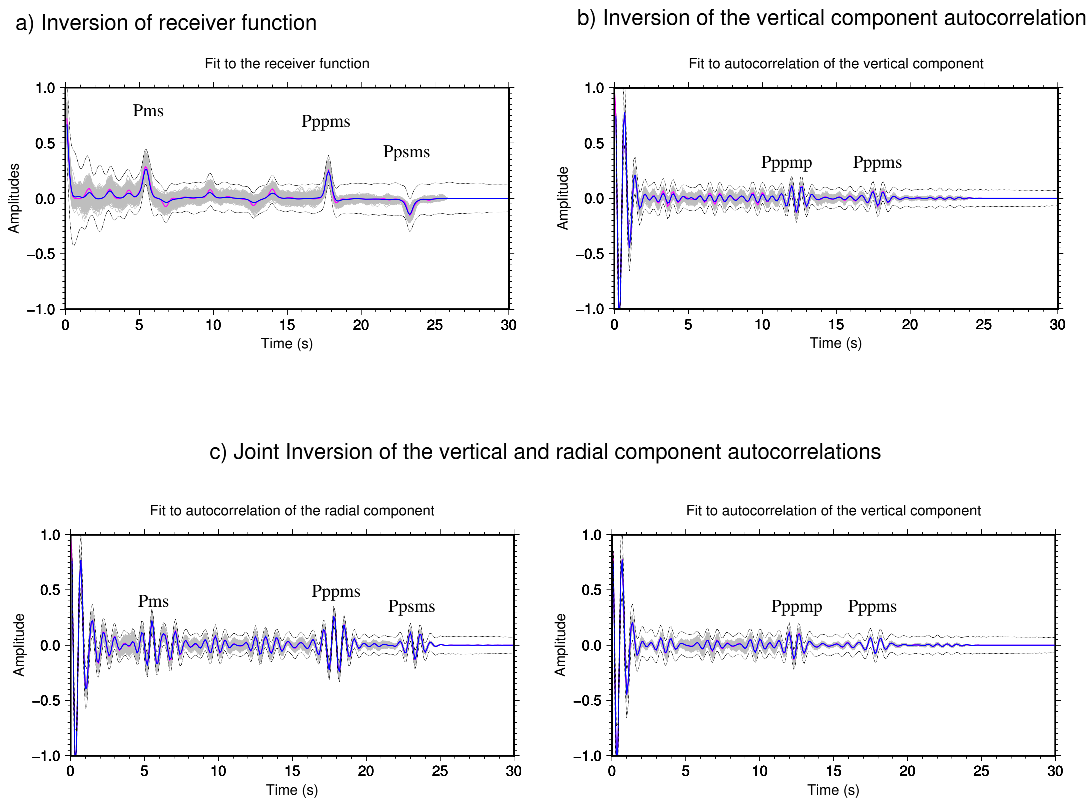

Figure 3. Synthetic inversions of a four-layered model with a ten-layered parameterization. Fits to data for a) inversion of the RF, b) inversion of the autocorrelation of the teleseismic P-wave coda recorded on the vertical component, c) joint inversion of autocorrelations of the teleseismic P-wave coda recorded on the vertical and radial components. Magenta waveforms are synthetic data and the blue waveform shows the mean of the best 2000 accepted predicted data (gray waveforms). The black dashed lines are the three standard deviation bounds (3σ) for the data. The Pms, Pppms, Pppmp and Ppsms phases associated with the Moho are also marked on the top of waveforms.

4 Joint Inversion of Field Data (central Australia)

Following the synthetic tests, we applied the new joint inversion method on field data recorded on a series of broadband seismic sensors deployed along a north-south profile (BILBY) in central Australia, comprised of 25 broadband seismic sensors operated between August 2008 and February 2011. This profile spans over 1000 km from the south of Australia to the north of the Australian continent, cutting several east-west trending geological domains of central Australia including the Gawler Craton, Eromanga and Officer Basins (in the Nawa Domain of the Gawler Craton), Musgrave Province, Amadeus Basin, Arunta Block and Georgina Basin (Figure 4). In the following sections, we first summarize the data processing and then discuss the results.

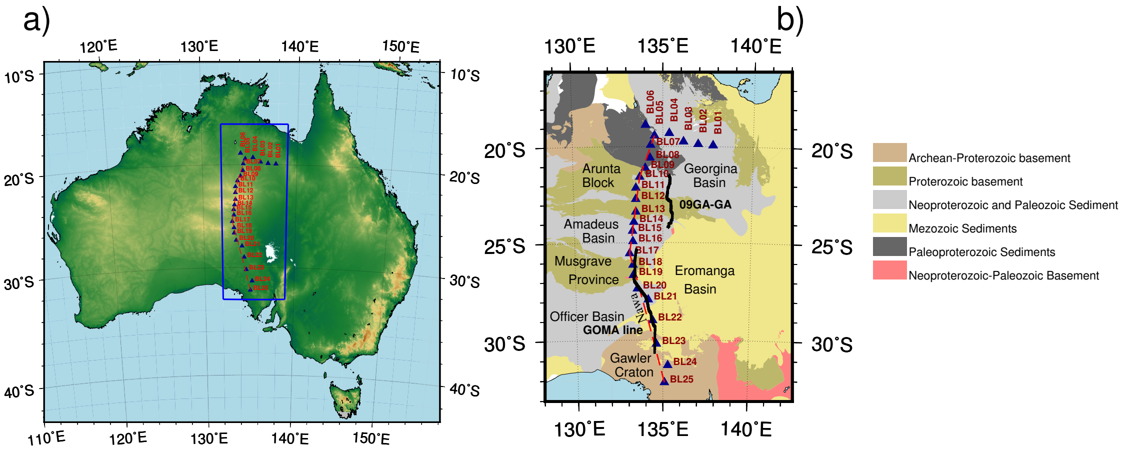

Figure 4. a) The BILBY experiment seismic stations are marked on the topographic map of Australia. The blue box shows the area shown in the right sub-figure (b) where the locations of the seismic stations and the GOMA and 09GA active seismic reflection lines are superimposed on the main geological units of central Australia. The crustal properties (shown in Figure 8) are extracted along the red dashed line.

4.1 Data Processing and Selection Criteria

In this study, we follow the approach of Tork Qashqai et al. (2019) for data selection and processing. We use teleseismic P-wave coda associated with events with magnitude greater than 5.5 and epicentral distances between 30° and 90° recorded by the vertical and radial components of broadband seismic stations along the BILBY profile. The chosen time window for P-wave coda is 10-70 s (tapering is applied) after the onset of the theoretical P-wave arrivals predicted by the ak135 model (Kennett et al., 1995). Only the first 30 seconds of this time window is used in the optimization of the joint inversion (when comparing the predicted and observed autocorrelations). Previous studies showed that there is coherent, prominent and stable scattered energy with comparable phase velocity to the direct P or PP phases in teleseismic P-wave coda (Aki, 1982; Dainty, 1990; Sens-Schönfelder et al., 2015; Kennett & Fichtner, 2020)[and see text S3 and Figures S8-S57 in the supporting information]. We remove the mean and trend of each record, and reject bad quality records (extremely noisy records, those with data gaps and short recording length), and then resample the data to 10 Hz.

To retrieve the equivalent local reflection responses below each seismic station, we apply a first-order Butterworth band-pass filter in the frequency range of 1 and 2 Hz before and after the autocorrelation, and then normalize amplitudes to unity. For both the radial and vertical components, we stack the autocorrelation waveforms from multiple events (after the move-out correction; see section 4.2) to increase the signal-to-noise ratio and suppress the source effects on reflection seismograms (Claerbout, 1968). We note here that one may need at least 30 events (for a simple structure) to 150 events (for a complex structure) to estimate a consistent velocity structure to that estimated from an inversion whose input (stacked autocorrelation) is calculated from all available events (Tork Qashqai et al., 2019, see supporting information). Tork Qashqai et al. (2019, see supporting information) showed that phases such as reflections from the core-mantle boundary (PcP) can contaminate our selected time window. They showed via synthetic calculations that the PcP reflections arrive in our selected time window of the P-wave coda at epicentral distances between 63° and 77° (slowness of 0.059-0.05 s/km). These core-mantle reflections can be considered as crustal reflections by the inversion. However, in this study, the average slowness for each seismic station is greater than 0.06 s/km. Furthermore, PcP reflections are suppressed by the move-out correction and stacking processes. Therefore, we believe their effect in our inverse modeling is negligible.

We note that for inversion to be robust, one needs to be cautious in describing the data uncertainties in the probabilistic inversion framework because the solution of the inverse problem is not unique. In the Bayesian joint inversion, for each station, we used (1σ) bounds of the variability (observational uncertainties/standard deviations) of the raw (observed) autocorrelations as 1σ values (σ_d^i and σ_d^j in equation (4)). One may argue that the observed data are the stacked autocorrelations and the standard deviations of them (can be estimated using the bootstrap resampling (Efron & Tibshirani, 1991)) should be used instead of the standard deviation of the observed autocorrelations. In the supporting information (text S1 and text S2, Figures S2-S7), we demonstrate with synthetic inversion tests that it will be near impossible to recover the true or synthetic model if the standard deviation of the stacked (mean) autocorrelation is used as data uncertainty in the probabilistic inversion framework.

4.2 Pre-stack move-out correction of the autocorrelation waveforms

Traveltimes of converted and reverberation phases (e.g., direct Ps or Pms, Pppmp, Pppms and Ppsms) in the autocorrelations of teleseismic P-wave coda are a function of the incident angle (slowness) of the impinging seismic wave. Tauzin et al. (2019) showed that for slowness values between 0.04 and 0.08 s/km, and for a simple model consists of a horizontal one-layer crust over a half-space mantle, the downgoing P and S-waves in the crust impinging on the Moho with an incident angle vary between 15 and 35° for P-waves, and between 10 and ~ 18 ° for S-waves. These incident angles over the range of slownesses (e.g., 0.04-0.08 s/km) introduce a move-out (or shift) in the traveltime of the converted and reverberation phases on the radial and vertical autocorrelations. Therefore, the converted and reverberated phases in the autocorrelations of the teleseismic P-wave coda need to be corrected for their move-out before the stacking. This is an important step because if no move-out correction is applied to the autocorrelations prior to the stacking, the misalignment of the phases can potentially weaken and broaden the amplitudes of the stacked waveforms. Thus, the signal-to-noise ratio will not be improved and the stacking becomes destructive which is particularly more severe when working with high-frequency signals (Wang et al., 2020). In the presence of a thick crust, and in the case of having a broad range of epicentral distances, this move-out is larger. This is shown in Figures 5a and 5c with synthetic autocorrelations with slowness values between 0.04 and 0.08 s/km. The autocorrelations are calculated using a simple synthetic (horizontal) one-layer crust (with thickness of 50 km) over an upper mantle half-space.

Since there might be more than one layer in the crust, we use the AuSREM crustal model (Salmon et al., 2012) and discretize it in fine layers below each seismic station. Then for each autocorrelation trace, the relative traveltimes of the direct P-to-S conversion (Pms), and the three crustal reverberations phases (Pppmp, Pppms and Ppsms) with respect to the primary P-wave are approximated by the following equations (Chen & Niu, 2013; Sun & Kennett, 2016; Zhu & Kanamori, 2000):

$$t_{0p1s} = \sum_{i=0}^{N} \left(\sqrt{\frac{1}{(V_s)_i^2} - p^2} - \sqrt{\frac{1}{(V_p)_i^2} - p^2} \right) dz_i \tag{5}$$

$$t_{3p0s} = \sum_{i=0}^{N} 2 \left(\sqrt{\frac{1}{(V_p)_i^2} - p^2} \right) dz_i \tag{6}$$

$$t_{2p1s} = \sum_{i=0}^{N} \left(\sqrt{\frac{1}{(V_s)_i^2} - p^2} + \sqrt{\frac{1}{(V_p)_i^2} - p^2} \right) dz_i \tag{7}$$

$$t_{1p2s} = \sum_{i=0}^{N} 2 \left(\sqrt{\frac{1}{(V_s)_i^2} - p^2} \right) dz_i \tag{8}$$

Naming of the arrival times of the above phases, $t_{\mathbf{m}p\mathbf{n}s}$, follows the convention used by Chen and Niu (2013) and Niu and James (2002), where **m** and **n** denote numbers of P and S-wave legs in the crust, i denotes layer's number, N is the total number of layers in the crust, p is the apparent horizontal slowness of the primary incident plane P-wave, and dz_i, $(V_p)_i$ and $(V_s)_i$ represent the thickness, P-wave and S-wave velocities of each fine layer in the AuSREM model, respectively.

For the move-out correction of Pms, Pppmp, Pppms and Ppsms phases, a reference slowness needs to be chosen, at which the time scale of the radial and vertical autocorrelations remains unchanged. Following equations (2) to (5) and using the AuSREM crustal model, the time scales of the radial and vertical autocorrelations are calculated for all slowness values including the reference slowness. The calculated time scales of autocorrelations are either stretched and compressed with respect to the time scale of the reference slowness. In this study, the mean values of all slowness values for all of the seismic stations vary between 0.064 and 0.066 km/s. Therefore, a fixed slowness value of 0.065 s/km is chosen as a reference slowness for the move-out corrections. We adopt and modify the "four-pin" approach developed by Chen and Niu (2013) to perform the move-out corrections. Our move-out correction differs from the "four-pin" approach in that we cut the autocorrelation traces into the following five segments (a "five-pin" approach): 1) $0 <$ t $\leq t_{0p1s}$, 2) $t_{0p1s} <$ t $\leq t_{3p0s}$, 3) $t_{3p0s} <$ t $\leq t_{2p1s}$, 4) $t_{2p1s} <$ t $\leq t_{1p2s}$, and 5) t $> t_{1p2s}$. For each segment, we stretch/contract the time scale of each autocorrelation segment with respect to the corresponding time segment in the time scale of the reference slowness.

The stacked radial and vertical autocorrelations for all stations with and without applying the move-out correction are given the supporting information (Figures S106-S155).

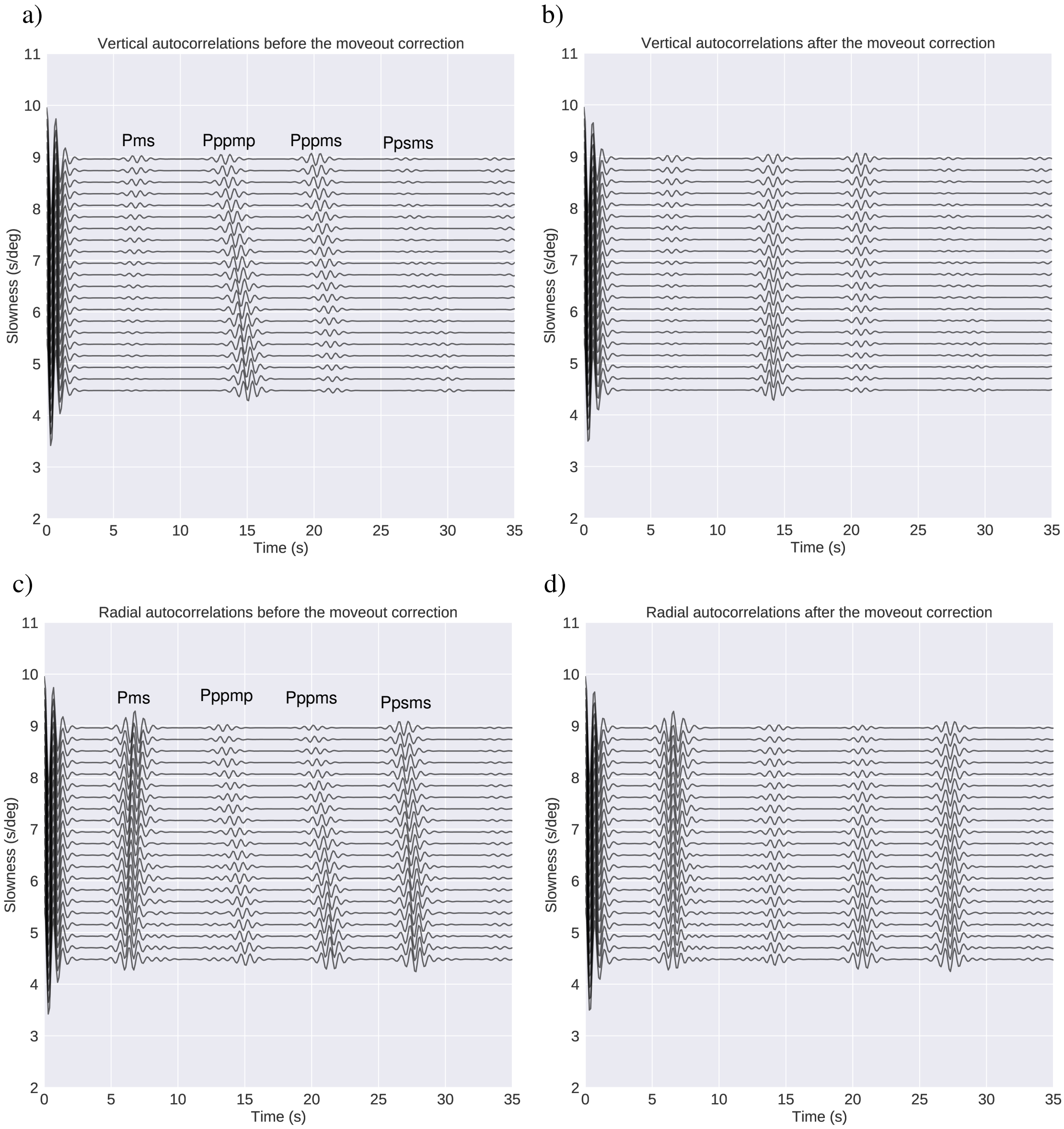

Figure 5. Synthetic vertical autocorrelations a) before and b) after the move-out correction. Synthetic radial autocorrelations c) before and d) after the move-out correction. The approximate locations of the expected seismic phases are also marked in a) and c). Autocorrelations are in the range of slowness between 4.4-8.8 s/deg (0.04 and 0.08 s/km) but the Y-axis is re-scaled for better visualization of the move-out of the converted and reverberated phases.

4.3 1-D Examples

This section represents two example results obtained from the joint autocorrelation inversions for stations BL22 (Figure 6) and BL05 (Figure 7). Moho depths and their 1σ uncertainties inferred from our approach for all the stations are given in Table S1 in the supporting information. Locations of all the stations, including BL22 and BL05 are given in Figures 4,6, and Figure 7. Station BL22 is located in the younger Officer Basin. Figure 6 shows the posterior distributions of the V_p/V_s ratio, V_p and V_s in the forms of density plots, as well as the fits to the observed data (Figures 6a and 6b) for this station. Figure 6a shows that both the observed vertical and radial component autocorrelations are well fitted by the joint inversion. In density plots, the high probability areas are displayed with hot colors, and show five to six major velocity jumps in the crust at depths of approximately 4 km, 10 km, 15 km (only for V_p), 20-27 km, and 35 km (only for V_s) and 38 km where the latter is associated with the Moho depth. The V_p/V_s ratio plot shows values < 1.7 for the first and third crustal layers and values between 1.75 and 1.95 for the V_p/V_s in the second crustal layer and the layers below 10 km.

Results of the inversion for station BL05 are displayed in Figure 7. The thinnest crust (37 km) in this study is found beneath this station in the Georgina Basin-Davenport Range region (Table S1). As can be seen, the crustal models contained in the posterior distribution explain well the autocorrelations of the radial and vertical components. Overall, the probability density plots of the V_p and V_s structures show that the crust can be characterized with four major layers, where the velocity jumps at the top and the lower crust are relatively sharp. The shear-wave structures (V_s) for both stations BL05 and BL22 show a gradational transition across the Moho depth.

The models contained in our posterior distributions of the crustal properties generally explain well most of the observed data along the BILBY transect. However, the observed data for stations BL23 and BL24 are not well fitted by the joint inversion. We provide the results of the joint inversion including fit to the data for the other stations in the supporting information (Figures S58-S80). The evolution of the misfit throughout the MCMC joint inversion for each of the stations is also given in the supporting information (Figures S81-S105).

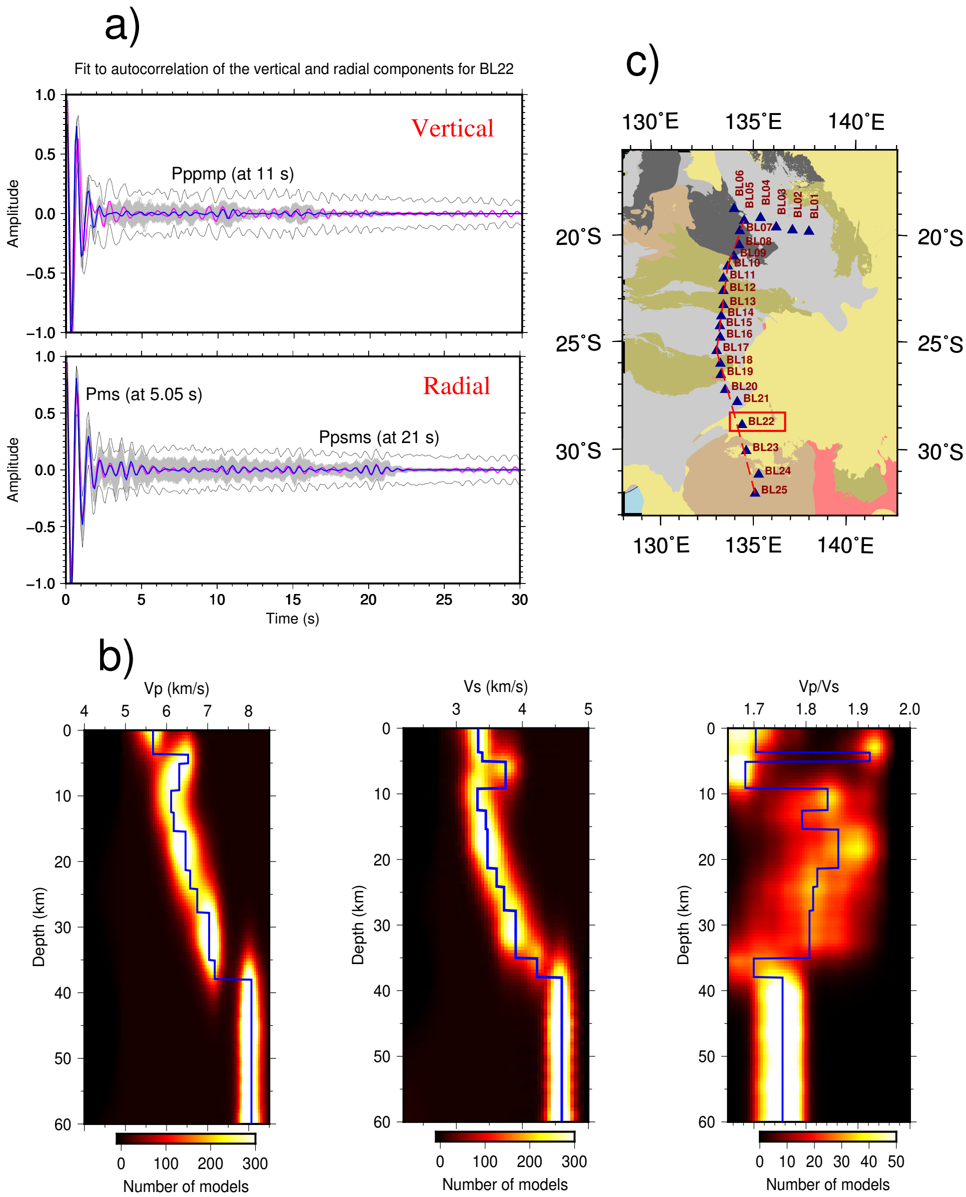

Figure 6. Results of the joint inversion of field measurements for station BL22. a) fit to the autocorrelation of the vertical and radial components, b) Density plot of V_p, V_s and the V_p/V_s ratio, c) The location of station BL22 is highlighted with a red box on the map of the study area. In the density plots, the mean values of the best 2000 accepted models in the posterior distributions are displayed with blue colors. In plots showing the fits to autocorrelations of the radial and vertical components, magenta represents the observed data and the mean of the best 2000 accepted predicted data (grays) is given by blue. The black dashed lines in a) are the one standard deviation bounds obtained during the stacking of the data. The Pms, Pppmp and Ppsms phases associated with the Moho are calculated using the velocity models in b) and marked on the radial and vertical autocorrelation waveforms.

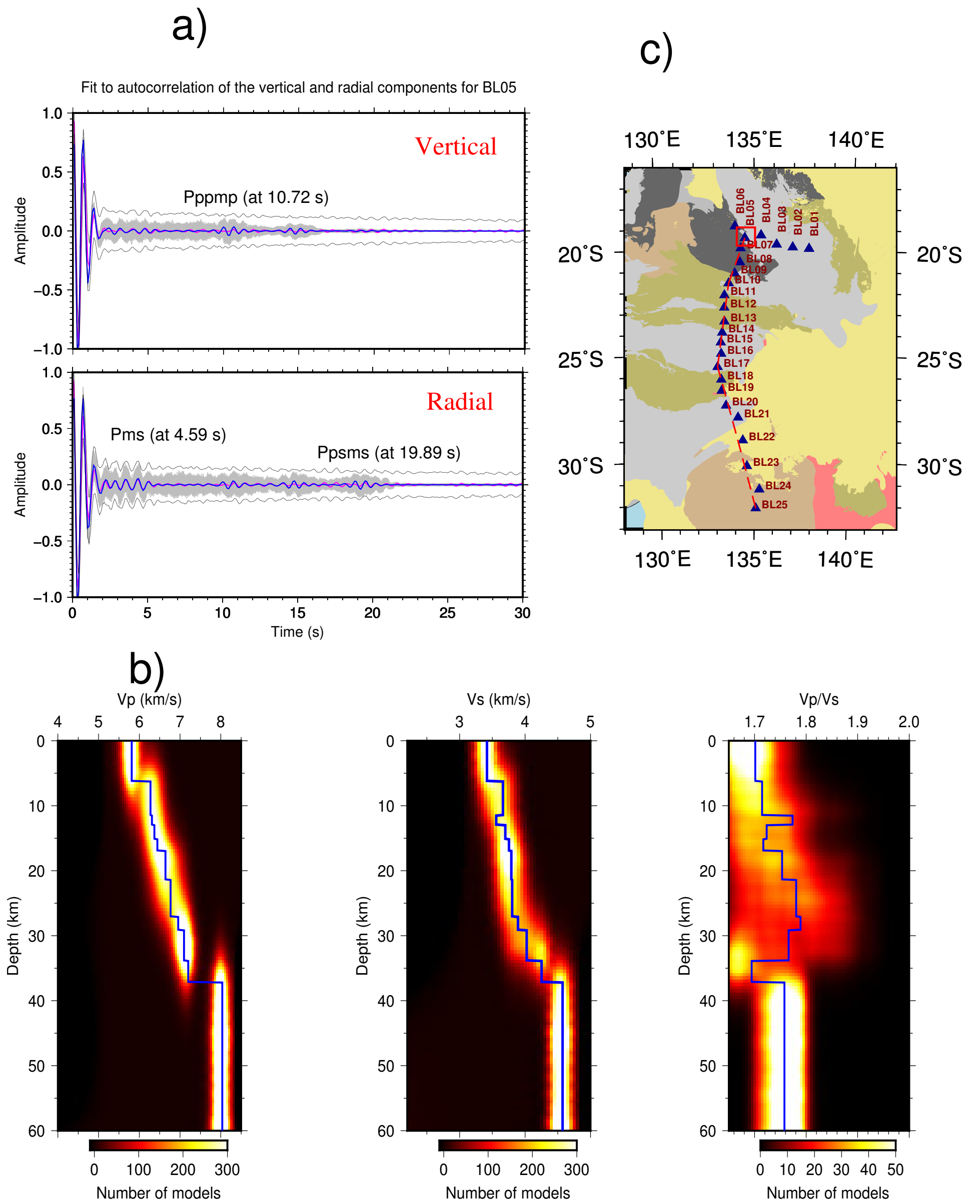

Figure 7. Results of the joint inversion of field measurements for station BL05. a) fit to the autocorrelation of the vertical and radial components, b) Density plot of V_p, V_s and the V_p/V_s ratio, c) The location of station BL05 is highlighted with a red box on the map of the study area. In the density plots, the mean values of the best 2000 accepted models in the posterior distributions are displayed with blue colors. In plots showing the fits to autocorrelations of the radial and vertical components, magenta represents the observed data and the mean of the best 2000 accepted predicted data (grays) is given by blue. The black dashed lines in a) are the one standard deviation bounds obtained during the stacking of the data. The Pms, Pppmp and Ppsms phases associated with the Moho are calculated using the velocity models in b) and marked on the radial and vertical autocorrelation waveforms.

5 2-D Results and Discussion

5.1 Sections of Crustal Properties

The mean values of the posterior distributions of the V_p, V_s and V_p/V_s associated with individual stations are interpolated to create sections of the crustal properties along the BILBY transect (Figure 8). The transect which is used to extract these sections of the crustal properties is shown by a red dashed line in Figure 4. The Moho depth estimated directly from the joint inversion is also marked with a continuous black line in Figure 8 and compared with the previous studies (section 5.2). Our modeling results include many detailed features but only the large-scale and most robust features are discussed here. Before we point out some systematic variations of the crustal properties, it is useful to briefly describe the importance of having knowledge of both V_p and V_s structures.

Understanding of both crustal V_p and V_s (e.g., V_p/V_s ratio) is of great importance to discriminate between different crustal materials. The V_p/V_s ratio in the crust usually varies from ~ 1.50 for felsic rocks (e.g., quartzite) to ~ 2.12 for unconsolidated sediments and mafic or ultramafic materials (e.g., serpentinite) (Christensen, 1996). Any major increase or decrease in abundance of either end-member has a dominant effect on the V_p/V_s ratio of the crustal layers. However, we note that several mafic and ultramafic lithologies have relatively low V_p/V_s ratios (Christensen, 1996). In addition to the above caveats, cracks with small volumes of aqueous fluids and the presence of gas/air bubbles in melt-bearing materials can also reduce the V_p more efficiently than V_s, thus decreasing the V_p/V_s ratio (Takei, 2002; Caricchi et al., 2008; Nakajima et al., 2001; Tripoli et al., 2016). The existence of fluid and/or melt, however, increase the V_p/V_s ratio (Takei, 2002; Nakajima et al., 2001).

Several important features can be inferred from the sections of the Vp, Vs and the V_p/V_s ratio, which we believe they are likely to be robust. The crustal V_p and V_s sections show dominant low velocities at depths less than 30 km along the line whereas depths greater than 30 km are mainly characterized with higher velocities. The V_p/V_s section shows a very complex pattern of high and low values, where the high V_p/V_s values at depths greater than 10 km are mostly localized beneath locations where the crustal blocks interact (e.g., across the transition from one domain to another). Another observation is that the dominant crustal V_p/V_s ratio variation is consistent with geological units. For example, the shallow crust below the Georgina and Amadeus Basins is dominated by large V_p/V_s ratios. This correlation is also observed in the average V_p/V_s ratios estimated using the inversion of receiver functions and the H-K approach (Sippl, 2016). In the middle crust of the Nawa Domain (Officer Basin) and the Gawler Craton, a high-velocity layer (which has a low V_p/V_s ratio) lies between the low-velocity layers (featuring high V_p/V_s ratios).

5.2 Moho structure

Recently, several studies have discussed the crustal structure of central Australia using either passive seismic data recorded by the stations along the BILBY experiment (Sippl, 2016; Thompson et al., 2019), or deep seismic reflection data. Geoscience Australia conducted several deep seismic sounding profiles with 20 s recording time across Australia (Kennett & Saygin, 2015; Kennett. et al., 2016) to better map the crustal structure and geodynamic evolution of the major geological provinces of Australia. Korsch and Doublier (2016) interpreted the major crustal boundaries and Moho across several regions in Australia, including along the GOMA and 09GA-GA seismic lines in central Australia (see Figure 4 for their locations). Among them, the GOMA deep seismic lines approximately overlap with parts of the BILBY transect (between 31°S and 25°S).

In Figure 8, we compare our Moho estimates (continues black line) with the Moho depths estimated from RFs (Sippl, 2016), the AusMoho model (Kennett. et al., 2011), and the inversion of the autocorrelation of the vertical component (Tork Qashqai et al., 2019). In Figure 9, we also compared our Moho estimates (dashed black lines) with those interpreted from the deep seismic reflection (dark green line) method (Korsch & Doublier, 2016, GOMA line). The Moho values obtained from this study are converted to their corresponding two-way travel time using our inverted P-wave velocity model (Figure 8a) to be comparable with the Moho depth interpreted from the migrated seismic section obtained from the deep seismic reflection method.

Moho varies between 37 km and 53 km along the BILBY transect. The crust beneath the Musgrave Province, Officer Basin and Arunta Block is characterized with a Moho uplift, which might be due to the presence of crustal-scale faults and shear zones [e.g., Redbank shear zone in Arunta block (Sippl, 2016; Goleby et al., 1989; Lambeck & Penney, 1984; Lambeck et al., 1988)]. A distinct and systematic pattern of the Moho variation is recognizable along the transect across the crustal domains. For example, the Moho is deep in the Georgina Basin and gets shallower beneath the Arunta block. It then gets deeper towards the Amadeus Basin, uplifted in the Musgrave province and the Officer Basin, reaches 41 km and 38 km beneath stations BL19 and BL22, respectively. The Moho gets deeper below stations BL23 (53 km), BL24 (51 km) and BL25 (46 km) in the Gawler Craton at the southern part of the BILBY passive seismic array.

Sippl (2016) reported a new Moho offset between stations BL09/BL08 and BL07, and imaged a crustal thickening of about 10 km from south to north (red horizontal bars in Figure 8). Sippl argued that this offset can be caused by a large-scale crustal fault that has not been imaged previously. We also image such a Moho offset from station BL09 to stations BL08 and BL07. This is also consistent with results obtained with the virtual deep seismic sounding method (Thompson et al., 2019). Since our approach relies on the 1-D Earth assumption, any existing crustal-scale fault cannot be clearly imaged when creating a pseudo 2-D profile by interpolation of the 1-D structures. However, the velocity models exhibit some large-scale planar structures dipping southward or northward which might be related to some deep large-scale penetrating faults/structures imaged with the active seismic method (Korsch & Doublier, 2016).

From Figure 9, the estimated traveltimes of the seismic waves reflected back from the Moho in our study are mostly less than those interpreted from the active seismic reflection method which can be due to a different velocity model being used to produce the migrated section. A large station interval in the passive seismic recording of the BILBY profile and the higher spatial resolution of the deep seismic reflection line can be other reasons for this difference. In this study, the Moho values between stations are estimated by interpolation of the 1-D estimates. However, the general trend of our Moho model in the time domain in the south of the Amadeus Basin follows the long-wavelength pattern of Moho interpreted from the deep seismic reflection sounding along the GOMA seismic line (Figure 9). The trend of the Moho structure from the active seismic, AusMoho model, the inversion of the autocorrelation of the vertical component and from our approach beneath the Officer Basin shows southward thinning of the crust (from stations BL20 to station BL22 in Figures 8-9). In contrast, the crust thickens toward the Gawler Craton in the south of station BL22 and reaches $\sim$ 50 km below station BL23, where a crustal-scale fault has been interpreted to cut and displace the Moho (Korsch & Doublier, 2016). The traveltimes of the seismic waves reflected from Moho, estimated from our velocity model, are closer to the change of the reflectivity at the base of the crust below most of the stations (e.g., station BL17, BL18, BL19, station BL23, and between stations BL21 and BL22).

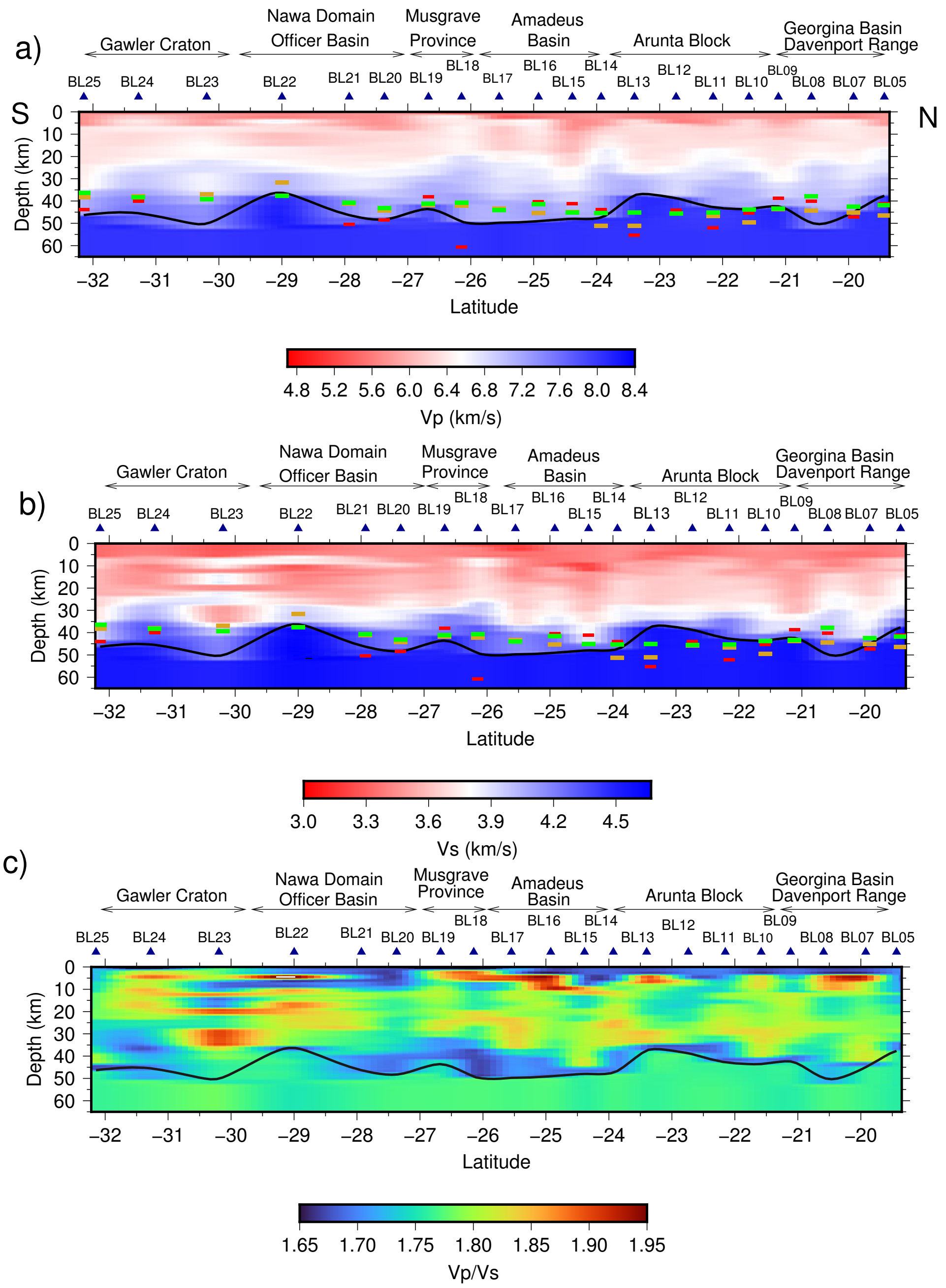

Figure 8. Sections of crustal properties inferred from combining the 1-D joint inversion results along the red transect shown in Figure 4. a) V_p, b) V_s, and c) V_p/V_s. The locations of seismic stations along the transect (red dashed line in Figure 4) are marked by blue triangles. The main geological units and crustal blocks are also indicated on top of the station codes. The Moho structure obtained in this study is shown by a black line. The Moho depth values estimated by the H-κ stacking method (Sippl, 2016, red thick horizontal bars) and the inversion of the vertical component autocorrelation (Tork Qashqai et al., 2019, light brown thick horizontal bars) are also plotted on the V_p and V_s sections for comparison. Moho estimates from the AusMoho model (Kennett. et al., 2011) are represented by green thick horizontal bars.

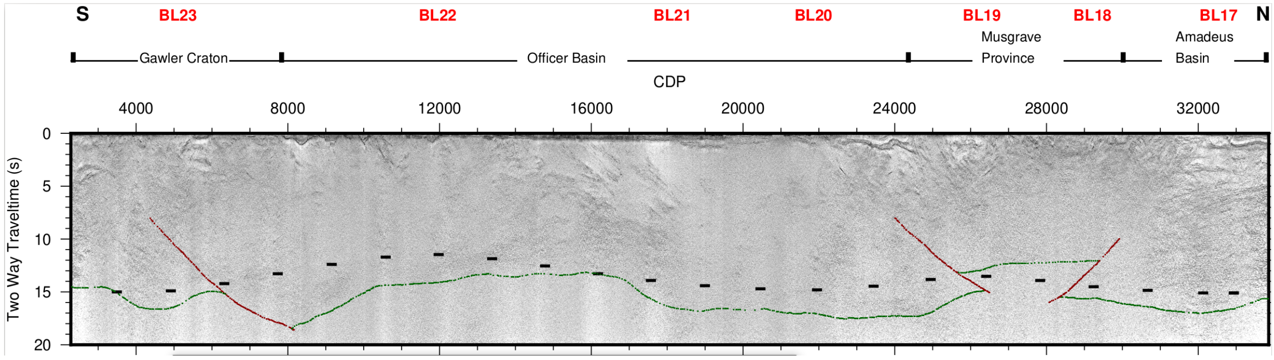

Figure 9. The Moho structure imaged by our joint inversion approach (black horizontal bars) is superimposed on the Gawler-Officer-Musgrave-Amadeus (GOMA) migrated seismic reflection section (Maher, 2010), and compared with the Moho structure interpreted from the deep seismic reflection method (Korsch & Doublier, 2016, shown by the green color). The major crustal-scale faults penetrating to the base of the crust are indicated by the brown color (Korsch & Doublier, 2016).

6 Conclusion

Unlike the P-to-S RFs, where main P-waves are attenuated by the deconvolving vertical component (P) seismogram from the radial (S_v) component, autocorrelations of the radial and vertical components retain P-waves as well as all other phases such as P-to-S phases (as in RFs). Therefore, the joint inversion of the radial component autocorrelation with autocorrelation of the vertical component can account for the variability of both V_p and V_s structures. We introduce a new joint inversion approach to simultaneously estimate V_p, V_s, and V_p/V_s ratio structures below a seismic station utilizing both the vertical and radial component autocorrelations of the teleseismic P-wave coda. We design and run a series of synthetic inversion tests to examine the feasibility of applying this approach. Results of the tests suggest that this approach can provide a significant improvement in the estimation of the crustal properties compared to the inversion of either the teleseismic radial RFs or the autocorrelation of the vertical component.

We successfully applied this technique on passive seismic data recorded along a north-south transect in central Australia to image and characterize the crustal blocks and their properties (V_p, V_s, Moho and V_p/V_s ratio) simultaneously. This study provides the first comprehensive joint estimates of all crustal properties for the BILBY seismic transect. The joint inversion of the radial and vertical autocorrelations of the teleseismic P-wave coda has significant implications for characterizing the V_p/V_s ratio, which is a good indicator of crustal composition. Velocity models show large-scale structures dipping northward and southward at some locations that might have caused the Moho offsets reported along the line. The overall trend of the Moho structure along the profile is quite compatible with the Moho depth estimated from the previous studies, including those interpreted from the migrated seismic reflection section (GOMA), with the exception in the north of Amadeus Basin, where inferred Moho depths shows some level of variability. The trend of the traveltimes of the reflection phases associated with the Moho, estimated from our velocity model, to a large extent, follows the general reflectivity character of the Moho reflections at the base of the crust. This demonstrates the feasibility of our joint inversion method to provide complementary information on the crustal structure. The new joint inversion approach is more cost-effective than the deep reflection profiling method and can be used to obtain additional information about the deep crust, especially at depths where the deep seismic reflection method has penetration problems.

Acknowledgments

This research was funded by the Deep Earth Imaging Future Science Platform, CSIRO. Inversions were performed using the Pearcey High-Performance Computing (HPC) cluster of the Commonwealth Scientific and Industrial Research Organization (CSIRO). Seismic data were retrieved from the AusPass archive (`http://auspass.edu.au/`) under a Creative Commons Attribution 4.0 International license. ObsPy (`https://doi.org/10.1785/gssrl.81.3.530`) were used to download and process seismic data. Python Matplotlib packages (`https://matplotlib.org/`) and the Generic Mapping Tools (Wessel et al., 2013) were used to plot the figures. The processed GOMA seismic reflection section can be downloaded from the Geoscience Australia portal (`http://pid.geoscience.gov.au/dataset/ga/70579`) under Creative Commons Attribution 4.0 International Licence. We thank Michael Doublier and Malcolm Nicoll from Geoscience Australia for sharing their deep seismic reflection interpretation with us. We thank Caroline Johnson and Peng Guo for reviewing an earlier version of the manuscript. We are grateful to the Editor, Michael Bostock, the Associate Editor and the two reviewers. The manuscript was greatly improved by constructive feedback and careful reviews by Benoit Tauzin, an anonymous reviewer, and the associated Editor.

References

Afonso, J. C., Rawlinson, N., Yang, Y., Schutt, D. L., Jones, A. G., Fullea, J., & Griffin, W. L. (2016). 3-d multiobservable probabilistic inversion for the compositional and thermal structure of the lithosphere and upper mantle: Iii. thermochemical tomography in the western-central u.s. *Journal of Geophysical Research: Solid Earth*, *121*(10), 7337-7370. doi: 10.1002/2016JB013049

Aki, K. (1982). Scattering and attenuation. *Bulletin of the Seismological Society of America*, *72*(6B), S319-S330. doi: 10.1785/BSSA07206B0319

Ammon, C. J. (1991). The isolation of receiver effects from teleseismic P waveforms. *Bulletin of the Seismological Society of America*, *81*(6), 2504-2510.

Andrés, J., Ayarza, P., Schimmel, M., Palomeras, I., Ruiz, M., & Carbonell, R. (2020). What can seismic noise tell us about the alpine reactivation of the iberian massif? an example in the iberian central system. *Solid Earth Discussions*, *2020*, 1–24. doi: 10.5194/se-2020-94

Ball, J. S., Sheehan, A. F., Stachnik, J. C., Lin, F. C., & Collins, J. A. (2014). A joint Monte Carlo analysis of seafloor compliance, Rayleigh wave dispersion and receiver functions at ocean bottom seismic stations offshore New Zealand. *Geochemistry, Geophysics, Geosystems*, *15*(12), 5051–5068. doi: 10.1002/2014GC005412

Becker, G., & Knapmeyer-Endrun, B. (2018). Crustal thickness across the Trans-European Suture Zone from ambient noise autocorrelations. *Geophysical Journal International*, *212*(2), 1237–1254. doi: 10.1093/gji/ggx485

Becker, G., & Knapmeyer-Endrun, B. (2019). Crustal thickness from horizontal component seismic noise auto- and cross-correlations for stations in Central and Eastern Europe. *Geophysical Journal International*. doi: 10.1093/gji/ggz164

Brocher, T. M. (2005). Empirical Relations between Elastic Wavespeeds and Density in the Earth's Crust. *Bulletin of the Seismological Society of America*, *95*(6), 2081–2092. doi: 10.1785/0120050077

Caricchi, L., Burlini, L., & Ulmer, P. (2008). Propagation of p and s-waves in magmas with different crystal contents: Insights into the crystallinity of magmatic reservoirs. *Journal of Volcanology and Geothermal Research*, *178*(4), 740 - 750. (Evolution, Transfer and Release of Magmas and Volcanic Gases) doi: https://doi.org/10.1016/j.jvolgeores.2008.09.006

Casas, J. A., Badi, G. A., Franco, L., & Draganov, D. (2020). Seismic interferometry applied to regional and teleseismic events recorded at planchón-peteroa volcanic complex, argentina-chile. *Journal of Volcanology and Geothermal Research*, *393*, 106805. doi: https://doi.org/10.1016/j.jvolgeores.2020.106805

Chen, Y., & Niu, F. (2013). Ray-parameter based stacking and enhanced preconditioning for stable inversion of receiver function data. *Geophysical Journal International*, *194*(3), 1682-1700. doi: 10.1093/gji/ggt179

Christensen, N. I. (1996). Poisson's ratio and crustal seismology. *Journal of Geophysical Research: Solid Earth*, *101*(B2), 3139–3156. doi: 10.1029/95jb03446

Claerbout, J. F. (1968). Synthesis of a layered medium from its acoustic transmission response. *Geophysics*, *33*(2), 264–269. doi: 10.1190/1.1439927

Dainty, A. (1990). Studies of coda using array and three-component processing. *Pure and Applied Geophysics (pageoph)*, *132*, 221–244.

Debski, W. (2010). Chapter 1 - probabilistic inverse theory. In R. Dmowska (Ed.), *Advances in geophysics* (Vol. 52, p. 1-102). Elsevier. doi: https://doi.org/10.1016/S0065-2687(10)52001-6

Efron, B., & Tibshirani, R. (1991). Statistical data analysis in the computer age. *Science*, *253*(5018), 390–395. doi: 10.1126/science.253.5018.390

Frasier, C. W. (1970). Discrete time solution of plane p-sv waves in a plane layered medium. *Geophysics*, *35*(2), 197-219. doi: 10.1190/1.1440085

Galetti, E., & Curtis, A. (2012). *Generalised receiver functions and seismic interferometry* (Vol. 532-535). Elsevier. doi: 10.1016/j.tecto.2011.12.004

Goleby, B. R., Shaw, R. D., Wright, C., Kennett, B. L., & Lambeck, K. (1989). Geophysical evidence for 'thick-skinned' crustal deformation in central Australia. *Nature*, *337*(6205), 325–330. doi: 10.1038/337325a0

Gorbatov, A., Saygin, E., & Kennett, B. L. N. (2013). Crustal properties from seismic station autocorrelograms. *Geophysical Journal International*, *192*(2), 861–870. doi: 10.1093/gji/ggs064

Gouveia, W. P., & Scales, J. A. (1998). Bayesian seismic waveform inversion: Parameter estimation and uncertainty analysis. *Journal of Geophysical Research: Solid Earth*, *103*(B2), 2759-2779. doi: https://doi.org/10.1029/97JB02933

Haario, H., Laine, M., Mira, A., & Saksman, E. (2006). Dram: Efficient adaptive mcmc. *Statistics and Computing*, *16*(4), 339–354. doi: 10.1007/s11222-006-9438-0

Haario, H., Saksman, E., & Tamminen, J. (2001). An adaptive metropolis algorithm. *Bernoulli*, *7*(2), 223–242.

Heath, B. A., Hooft, E. E., & Toomey, D. R. (2018). Autocorrelation of the Seismic Wavefield at Newberry Volcano: Reflections From the Magmatic and Geothermal Systems. *Geophysical Research Letters*, *45*(5), 2311–2318. doi: 10.1002/2017GL076706

Kennett., B. (2015). Lithosphere-asthenosphere p-wave reflectivity across australia. *Earth and Planetary Science Letters*, *431*, 225 - 235. doi: https://doi.org/10.1016/j.epsl.2015.09.039

Kennett., B., Saygin, E., Fomin, T., & Blewett, R. (2016). *Deep crustal seismic reflection profiling australia 1978-2015.* ANU Press and Geoscience Australia, Canberra. doi: http://dx.doi.org/10.22459/DCSRP.11.2016

Kennett, B. L. N. (1983). *Seismic wave propagation in stratified media.* Cambridge: Cambridge University Press.

Kennett, B. L. N., Engdahl, E. R., & Buland, R. (1995). Constraints on seismic velocities in the Earth from traveltimes. *Geophysical Journal International*, *122*(1), 108-124. doi: 10.1111/j.1365-246X.1995.tb03540.x

Kennett, B. L. N., & Fichtner, A. (2020). Scattering and stochasticwaveguides. In *Exploiting seismic waveforms: Correlation, heterogeneity and inversion* (p. 277–306). Cambridge University Press. doi: 10.1017/9781108903035.016

Kennett., B. L. N., Salmon, M., Saygin, E., & Group, A. W. (2011). AusMoho: The variation of Moho depth in Australia. *Geophysical Journal International*, *187*(2), 946–958. doi: 10.1111/j.1365-246X.2011.05194.x

Kennett, B. L. N., & Saygin, E. (2015). *The nature of the Moho in Australia from reflection profiling: A review* (Vol. 5). Elsevier. doi: 10.1016/j.grj.2015.02.001

Kennett, B. L. N., Saygin, E., & Salmon, M. (2015). Stacking autocorrelograms to map Moho depth with high spatial resolution in southeastern Australia. *Geophysical Research Letters*, *42*(18), 7490–7497. doi: 10.1002/2015GL065345

Kim, D., Brown, L. D., Árnason, K., Águstsson, K., & Blanck, H. (2017). Magma reflection imaging in Krafla, Iceland, using microearthquake sources. *Journal of Geophysical Research: Solid Earth*, *122*(7), 5228–5242. doi: 10.1002/2016JB013809

Kim, D., Keranen, K. M., Abers, G. A., & Brown, L. D. (2019). Enhanced Resolution of the Subducting Plate Interface in Central Alaska From Autocorrelation of Local Earthquake Coda. *Journal of Geophysical Research: Solid Earth*, 2018JB016167. doi: 10.1029/2018JB016167

Korsch, R. J., & Doublier, M. P. (2016). Major crustal boundaries of Australia, and their significance in mineral systems targeting. *Ore Geology Reviews*, *76*, 211–228. doi: 10.1016/j.oregeorev.2015.05.010

Lambeck, K., Burgess, G., & Shaw, R. D. (1988). Teleseismic travel-time anomalies and deep crustral structure in central Australia. *Geophysical Journal*, *94*(1), 105–124. doi: 10.1111/j.1365-246X.1988.tb03431.x

Lambeck, K., & Penney, C. (1984). Teleseismic travel time anomalies and crustal structure in central Australia. *Physics of the Earth and Planetary Interiors*, *34*(1-2), 46–56. doi: 10.1016/0031-9201(84)90083-9

Langston, C. A. (1979). Structure under Mount Rainier, Washington, inferred from teleseismic body waves. *Journal of Geophysical Research*, *84*(B9), 4749–4762. doi: 10.1029/JB084iB09p04749

Ludwig, W. J., Nafe, J. E., & Drake, C. L. (1970). *Seismic refraction, in the sea , a. e. maxwell (editor)* (Vol. 4). New York: Wiley-Interscience.

Maher, J. L. (2010). L190 Gawler-Officer-Musgrave-Amadeus Deep Crustal Seismic Survey, SA & NT, 2008. Stacked and Migrated Data and Images for 08GA-OM. *Geoscience Australia, Canberra*.

Mira, A. (2001). On Metropolis-Hastings algorithms with delayed rejection. *Metron - International Journal of Statistics*, *0*(3-4), 231-241.

Mosegaard, K., & Hansen, T. M. (2016). Inverse methods. In *Integrated imaging of the earth* (p. 7-27). American Geophysical Union (AGU). doi: https://doi.org/10.1002/9781118929063.ch2

Nakajima, J., Matsuzawa, T., Hasegawa, A., & Zhao, D. (2001). Three-dimensional structure of vp, vs, and vp/vs beneath northeastern japan: Implications for arc magmatism and fluids. *Journal of Geophysical Research: Solid Earth*, *106*(B10), 21843-21857. doi: 10.1029/2000JB000008

Nishitsuji, Y., Rowe, C. A., Wapenaar, K., & Draganov, D. (2016). Reflection imaging of the Moon's interior using deep-moonquake seismic interferometry. *Journal of Geophysical Research E: Planets*, *121*(4), 695–713. doi: 10.1002/2015JE004975

Niu, F., & James, D. E. (2002). Fine structure of the lowermost crust beneath the kaapvaal craton and its implications for crustal formation and evolution. *Earth and Planetary Science Letters*, *200*(1), 121-130. doi: https://doi.org/10.1016/S0012-821X(02)00584-8

Oren, C., & Nowack, R. L. (2017). Seismic body-wave interferometry using noise autocorrelations for crustal structure. *Geophysical Journal International*, *208*(1), 321–332. doi: 10.1093/gji/ggw394

Phạm, T. S., & Tkalčić, H. (2018). Antarctic Ice Properties Revealed From Teleseismic P Wave Coda Autocorrelation. *Journal of Geophysical Research: Solid Earth*, *123*(9), 7896–7912. doi: 10.1029/2018JB016115

Randall, G. E. (1989). Efficient calculation of differential seismograms for lithospheric receiver functions. *Geophysical Journal International*, *99*(3), 469–481.

doi: 10.1111/j.1365-246X.1989.tb02033.x

Romero, P., & Schimmel, M. (2018). Mapping the Basement of the Ebro Basin in Spain With Seismic Ambient Noise Autocorrelations. *Journal of Geophysical Research: Solid Earth*, *123*(6), 5052–5067. doi: 10.1029/2018JB015498

Ruigrok, E., & Wapenaar, K. (2012). Global-phase seismic interferometry unveils P-wave reflectivity below the Himalayas and Tibet. *Geophysical Research Letters*, *39*(11), n/a–n/a. doi: 10.1029/2012GL051672

Salmon, M., Kennett, B. L. N., & Saygin, E. (2012). Australian Seismological Reference Model (AuSREM): crustal component. *Geophysical Journal International*, *192*(1), 190-206. doi: 10.1093/gji/ggs004

Saygin, E., Cummins, P. R., & Lumley, D. (2017). Retrieval of the P wave reflectivity response from autocorrelation of seismic noise: Jakarta Basin, Indonesia. *Geophysical Research Letters*, *44*(2), 792–799. doi: 10.1002/2016GL071363

Sens-Schönfelder, C., Snieder, R., & Stähler, S. C. (2015). The lack of equipartitioning in global body wave coda. *Geophysical Research Letters*, *42*(18), 7483-7489. doi: https://doi.org/10.1002/2015GL065108

Sippl, C. (2016). Moho geometry along a north-south passive seismic transect through Central Australia. *Tectonophysics*, *676*, 56–69. doi: 10.1016/j.tecto.2016.03.031

Smith, T. J., & Marshall, L. A. (2008). Bayesian methods in hydrologic modeling: A study of recent advancements in markov chain monte carlo techniques. *Water Resources Research*, *44*(12). doi: 10.1029/2007WR006705

Sun, W., Fu, L.-Y., Saygin, E., & Zhao, L. (2018). Insights Into Layering in the Cratonic Lithosphere Beneath Western Australia. *Journal of Geophysical Research: Solid Earth*. doi: 10.1002/2017JB014904

Sun, W., & Kennett, B. L. (2016). Receiver structure from teleseisms: Autocorrelation and cross correlation. *Geophysical Research Letters*, *43*(12), 6234–6242. doi: 10.1002/2016GL069564

Takei, Y. (2002). Effect of pore geometry on vp/vs: From equilibrium geometry to crack. *Journal of Geophysical Research: Solid Earth*, *107*(B2), ECV 6-1-ECV 6-12. doi: 10.1029/2001JB000522

Tarantola, A. (2005). *Inverse problem theory and methods for model parameter estimation.* Philadelphia, PA, USA: Society for Industrial and Applied Mathematics.

Tauzin, B., Phạm, T., & Tkalčić, H. (2019). Receiver functions from seismic interferometry: a practical guide. *Geophysical Journal International*, *217*(1), 1–24. doi: 10.1093/gji/ggz002

Taylor, G., Rost, S., & Houseman, G. (2016). Crustal imaging across the North Anatolian Fault Zone from the autocorrelation of ambient seismic noise. *Geophysical Research Letters*, *43*(6), 2502–2509. doi: 10.1002/2016GL067715

Thompson, D. A., Rawlinson, N., & Tkalčić, H. (2019). Testing the limits of virtual deep seismic sounding via new crustal thickness estimates of the Australian continent. *Geophysical Journal International*. doi: 10.1093/gji/ggz191

Tibuleac, I. M., & von Seggern, D. (2012). Crust-mantle boundary reflectors in Nevada from ambient seismic noise autocorrelations. *Geophysical Journal International*, *189*(1), 493–500. doi: 10.1111/j.1365-246X.2011.05336.x

Tierney, L. (1994). Markov chains for exploring posterior distributions. *Ann. Statist.*, *22*(4), 1701–1728. doi: 10.1214/aos/1176325750

Tork Qashqai, M., Afonso, J. C., & Yang, Y. (2018). Physical state and structure of the crust beneath the western-central united states from multiobservable probabilistic inversion. *Tectonics*, *37*(9), 3117-3147. doi: 10.1029/2017TC004914

Tork Qashqai, M., Saygin, E., & Kennett, B. L. N. (2019). Crustal imaging with bayesian inversion of teleseismic p wave coda autocorrelation. *Journal of Geophysical Research: Solid Earth*, *124*(6), 5888-5906. doi: 10.1029/2018JB017055

Tripoli, B. A., Cordonnier, B., Zappone, A., & Ulmer, P. (2016). Effects of crystallization and bubble nucleation on the seismic properties of magmas. *Geochemistry, Geophysics, Geosystems*, *17*(2), 602-615. doi: 10.1002/2015GC006123

Vinnik, L. (1977). Detection of waves converted from p to sv in the mantle. *Physics of the Earth and Planetary Interiors*, *15*(1), 39-45. doi: https://doi.org/10.1016/0031-9201(77)90008-5

Wang, C., Tauzin, B., Pham, T.-S., & Tkalčić, H. (2020). On the efficiency of p-wave coda autocorrelation in recovering crustal structure: Examples from dense arrays in the eastern united states. *Journal of Geophysical Research: Solid Earth*, *125*(12), e2020JB020270. (e2020JB020270 10.1029/2020JB020270) doi: https://doi.org/10.1029/2020JB020270

Wessel, P., Smith, W. H. F., Scharroo, R., Luis, J., & Wobbe, F. (2013). Generic mapping tools: Improved version released. *Eos, Transactions American Geophysical Union*, *94*(45), 409-410. doi: 10.1002/2013EO450001

Zhu, L., & Kanamori, H. (2000). Moho depth variation in southern california from teleseismic receiver functions. *Journal of Geophysical Research: Solid Earth*, *105*(B2), 2969-2980. doi: https://doi.org/10.1029/1999JB900322